

TopoCL: Topological Contrastive Learning for Medical Imaging

Guangyu Meng¹ Pengfei Gu^{2*} Peixian Liang¹
 John P. Lalor^{1,3} Erin Wolf Chambers^{1*} Danny Z. Chen^{1*}

¹Dept. of Computer Science and Engineering, University of Notre Dame

²The University of Texas Rio Grande Valley

³Dept. of IT, Analytics, and Operations, University of Notre Dame

{gmeng, pliang, john.lalor, echambe2, dchen}@nd.edu, pengfei.gu01@utrgv.edu

Abstract

Contrastive learning (CL) has become a powerful approach for learning representations from unlabeled images. However, existing CL methods focus predominantly on visual appearance features while neglecting topological characteristics (e.g., connectivity patterns, boundary configurations, cavity formations) that provide valuable cues for medical image analysis. To address this limitation, we propose a new topological CL framework (TopoCL) that explicitly exploits topological structures during contrastive learning for medical imaging. Specifically, we first introduce topology-aware augmentations that control topological perturbations using a relative bottleneck distance between persistence diagrams, preserving medically relevant topological properties while enabling controlled structural variations. We then design a Hierarchical Topology Encoder that captures topological features through self-attention and cross-attention mechanisms. Finally, we develop an adaptive mixture-of-experts (MoE) module to dynamically integrate visual and topological representations. TopoCL can be seamlessly integrated with existing CL methods. We evaluate TopoCL on five representative CL methods (SimCLR, MoCo-v3, BYOL, DINO, and Barlow Twins) and five diverse medical image classification datasets. The experimental results show that TopoCL achieves consistent improvements: an average gain of +3.26% in linear probe classification accuracy with strong statistical significance, verifying its effectiveness. Code is publicly available.

1. Introduction

Medical image annotation is a resource-intensive process that requires specialized domain expertise, making it significantly more costly and time-consuming than labeling

*Corresponding authors. This research was supported in part by NSF Grants CCF-2444309 and CCF-2523787, AHA award 26AIREA1574568.

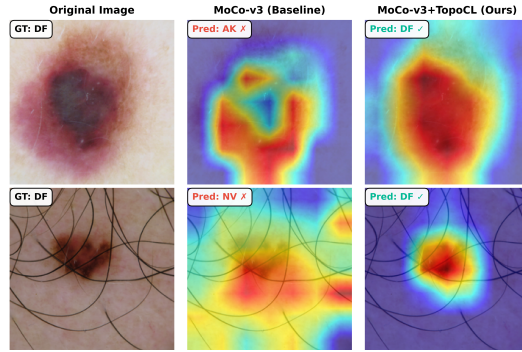


Figure 1. Visualization of failure cases corrected by TopoCL on ISIC2019 [39]. Two dermatofibroma (DF) cases are misclassified by the baseline MoCo-v3 [9] as actinic keratosis (AK, top) and melanocytic nevi (NV, bottom). MoCo-v3+TopoCL correctly classifies both as DF by capturing characteristic topological features: circular-to-oval boundary patterns with uniform internal connectivity (top) and radial pigmentation structures with a consistent boundary configuration despite hair overlay (bottom). Grad-CAM [35] heatmaps show that TopoCL focuses on lesion boundaries and internal structural patterns, while the baseline exhibits scattered attention on peripheral or irrelevant regions.

natural images [4, 22, 27, 33]. As a result, medical image datasets often suffer from severe label scarcity and substantial inter-observer variability [22, 33]. These labeling challenges fundamentally constrain supervised learning approaches, limiting model generalization and clinical applicability [3, 46]. Contrastive learning (CL) has emerged as a powerful approach to address these annotation limitations, enabling models to learn rich visual representations from abundant unlabeled data before fine-tuning for downstream tasks with minimal labeled samples [5, 8, 21, 37].

The core principle of CL is to apply data augmentations to create multiple views of each image, encode these views through deep neural networks, and learn representations that maximize agreement between different views of

the same image [8, 21]. Representative CL methods include SimCLR [8], MoCo-v3 [9], BYOL [17], DINO [5], and Barlow Twins [44], which employ learning objectives based on contrastive losses, momentum encoders, predictive learning, self-distillation, and redundancy reduction. These methods achieve impressive performance by capturing local appearance features such as textures, intensities, and color patterns. However, they fundamentally operate on pixel-level semantics and do not explicitly encode topological patterns (e.g., connectivity, holes, and boundary configurations), thus neglecting structural information useful for medical image analysis. As Fig. 1 shows, this limitation can lead to misclassifications of lesion types that differ primarily in boundary patterns, connectivity structures, or cavity formations but are “similar” in visual appearance. Such topological differences, captured by persistent homology, may be diagnostically critical but are largely overlooked by visual-only contrastive learning methods.

To address this gap, we propose **TopoCL**, a new general topological contrastive learning framework for medical images that augments standard contrastive learning with explicit topology preservation. Since standard CL augmentations provide no guarantee on structural preservation, we first introduce *topology-aware augmentations* that quantify and control topological perturbations using relative bottleneck distance computed on regions of interest. We then design a *Hierarchical Topology Encoder* that processes topological features across different dimensions (H_0 : connected components; H_1 : holes) through self-attention and cross-attention mechanisms to capture inter-dimensional structural relationships. Both the visual and topological encoders are pretrained independently using identical contrastive objectives. Finally, we employ an *adaptive Mixture-of-Experts (MoE) fusion module* to dynamically integrate their representations through five complementary experts (visual-only, topology-only, concatenation, gated blending, and cross-attention) using learned per-sample gating, producing the final topology-aware representations.

Our main contributions are as follows: **(1) Topology-aware augmentation design:** Our new systematic method for designing augmentations explicitly quantifies and controls topological perturbations. Using relative bottleneck distance on regions of interest, we produce weak and strong topological augmentations that preserve diagnostically relevant structures while providing sufficient topological diversity for contrastive learning. **(2) TopoCL framework:** We propose a new topology-enhanced CL framework with a Hierarchical Topology Encoder and an adaptive MoE fusion module for integrating topological priors into contrastive learning. **(3) Comprehensive validation:** We demonstrate consistent average accuracy improvements of +3.26% across five CL methods and five medical image classification benchmarks, with strong statistical significance (86%

of comparisons with $p < 0.05$ and 80% with $p < 0.001$). Our code is publicly available at <https://github.com/gm3g11/TopoCL>.

2. Related Work

Contrastive Learning in Medical Imaging. CL has become a powerful paradigm for learning visual representations from unlabeled images by maximizing the agreement between augmented views of the same instance [37]. Representative CL methods include SimCLR [8] with InfoNCE loss, MoCo-v3 [9] with momentum encoders, BYOL [17] with online-target asymmetry, Barlow Twins [44] with redundancy reduction, and DINO [5] with self-distillation. Despite their different loss formulations, these methods share the same fundamental principle of learning by comparing multiple views of the same input, and have been successfully applied to medical imaging [3, 40].

However, existing CL methods fundamentally learn visual appearance features from local pixel neighborhoods, overlooking global structural properties critical for medical image analysis. Their augmentation strategies (random cropping, color jittering, Gaussian blurring, etc.) were designed for visual appearances and do not characterize topological structures. Our work addresses these limitations by augmenting CL with explicit topological feature learning and topology-aware augmentations, providing a general enhancement scheme applicable to any CL method.

Topological Data Analysis for Medical Images. Appearance-driven CL methods can overlook geometric properties useful for medical image analysis [19, 20, 30], such as tissue components, glandular lumens, and lesion boundaries [14, 24]. Persistent homology (PH) [13] quantifies topology by tracking the births and deaths of connected components (H_0) and loops (H_1), summarizing them in persistence diagrams (PDs) with stability guarantees [7, 11]. A topological feature in an image I based on a filtration function is characterized by its birth time b and death time d , forming $\text{PD}(I) = \{(b_i, d_i)\}$. The bottleneck distance $d_B(\text{PD}_1, \text{PD}_2) = \inf_{\gamma} \sup_p \|p - \gamma(p)\|_{\infty}$ measures dissimilarity between two PDs via an optimal matching γ [11]. We employ cubical PH [42], extracting topological signatures from the pixel intensities of images.

Previous work applied PH to medical imaging for texture analysis [38], segmentation [1, 10, 18], tumor grading [24, 31], and supervised classification with architectures like PersLay [6] and PHG-Net [30]. These methods predominantly use topology as auxiliary losses or in labeled settings. Unlike these methods, our work integrates PH into contrastive self-supervised learning, introducing a Hierarchical Topology Encoder with cross-attention to capture relationships between H_0 and H_1 and designing topology-aware augmentations that control structural perturbations.

Feature Fusion Strategies. Effective integration of hetero-

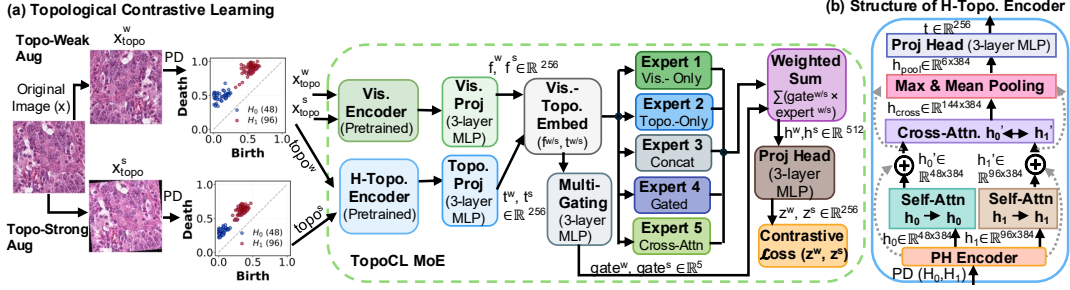


Figure 2. An overview of our TopoCL framework. (a) **Topological Contrastive Learning**: Given an input image x , we generate two views with topology-weak (x_{topo}^w) and topology-strong (x_{topo}^s) augmentations, and compute their persistence diagrams topo^w and topo^s . The visual encoder processes $x_{\text{topo}}^w, x_{\text{topo}}^s$ while the topology encoder processes $\text{topo}^w, \text{topo}^s$, with projection heads producing visual features f^w, f^s and topological features t^w, t^s . The TopoCL MoE module fuses these features through five experts (the colors distinguish the fusion strategies: Vis-Only, Topo-Only, Concat, Gated, and Cross-Attn) with learned gating weights, producing fused representations h^w, h^s . A projection head maps these to the final representations z^w, z^s , optimized via contrastive loss. (b) **The structure of H-Topo. Encoder**: It uses hierarchical self- and cross-attention to capture topological features from PDs with both H_0 and H_1 homology dimensions.

geneous features is critical for representation learning [26, 45]. Common strategies include concatenation [29], bilinear pooling [16], cross-attention [41], gated fusion [2], and Transformer-based fusion [28]. However, these fixed strategies assume that one approach is optimal for all inputs.

Mixture-of-Experts (MoE) methods [15, 36] provide a framework for adaptive computation by routing inputs to specialized sub-networks. While successful in language models and Vision Transformers [34], to the best of our knowledge, MoE has not been explored for fusing visual and topological features. Our work introduces the first MoE architecture for visual-topological feature fusion.

3. Method

Fig. 2 illustrates our TopoCL framework. Our approach enhances standard CL by incorporating topological features: We independently pretrain the visual and topology encoders, and then jointly fine-tune them with adaptive MoE fusion. Specifically, we present an overview of the framework in Section 3.1, the topology-aware augmentations in Section 3.2, hierarchical topology encoder in Section 3.3, and MoE fusion module in Section 3.4.

3.1. Overview

Given unlabeled medical images, $\mathcal{D} = \{x_i\}_{i=1}^N$, and a base CL method \mathcal{M} (e.g., SimCLR, MoCo-v3, BYOL), TopoCL enhances \mathcal{M} by incorporating topological features to learn effective representations. We adopt a pretraining-then-fusion strategy: We independently pretrain visual encoder f_v and topology encoder f_t , both using contrastive objective $\mathcal{L}_{\mathcal{M}}$ but with different augmentations. For visual pretraining, we apply standard augmentations (random crop, color jitter, Gaussian blur) to generate x_{vis}^w and x_{vis}^s (superscripts w and s indicate weak and strong views). For topology pretraining and joint fine-tuning, we apply topology-aware augmentations (Section 3.2) to generate x_{topo}^w and

x_{topo}^s . Independent pretraining ensures that each encoder learns feature-specific representations without interference, while joint fine-tuning aligns feature spaces for fusion.

Visual Encoder Pretraining. We generate x_{vis}^w and x_{vis}^s , and optimize the encoder parameters θ_v through a 3-layer MLP projection head g_v :

$$\theta_v^* = \arg \min_{\theta_v} \mathbb{E}_{x \sim \mathcal{D}} [\mathcal{L}_{\mathcal{M}}(g_v(f_v(x_{\text{vis}}^w)), g_v(f_v(x_{\text{vis}}^s)))].$$

Topology Encoder Pretraining. We generate x_{topo}^w and x_{topo}^s and compute their PDs via persistent homology: $\text{topo}^w = \text{PD}(x_{\text{topo}}^w)$ and $\text{topo}^s = \text{PD}(x_{\text{topo}}^s)$. We optimize the encoder parameters θ_t through a 3-layer MLP projection head g_t :

$$\theta_t^* = \arg \min_{\theta_t} \mathbb{E}_{x \sim \mathcal{D}} [\mathcal{L}_{\mathcal{M}}(g_t(f_t(\text{topo}^w)), g_t(f_t(\text{topo}^s)))].$$

Joint Fine-tuning. After pretraining, we integrate both encoders via an adaptive MoE module (TopoCL MoE in Fig. 2(a)) and jointly fine-tune all parameters, including the pretrained encoders f_v and f_t . We project both encoder outputs to a shared 256-dimensional embedding space through separate 3-layer MLP projection heads, yielding visual features $f^{w/s}$ and topological features $t^{w/s}$. These features are then fused through the MoE module and optimized using the contrastive loss $\mathcal{L}_{\mathcal{M}}$.

3.2. Topology-Aware Augmentations

Existing CL methods [8, 9, 17] use standard visual augmentation strategies designed to preserve visual appearances but do not explicitly control their effects on topological structures. However, topological features such as lesion boundaries and tissue connectivity are critical for medical image analysis [24, 25, 31], and visual-only augmentations can inadvertently alter these medically-relevant structures. To address this lack of topological control, we introduce topology-weak and topology-strong augmentations, which

Table 1. Topology-aware augmentation categories. All topological effects (except homeomorphism) are parameter-dependent.

Category	Operations	Topological Effect
Homeomorphism	Flips, rotations	Topology-preserving ($d_B^{\text{rel}} \approx 0$)
Boundary perturb.	Gaussian noise	Perturb boundary structures
Smoothing	Gaussian blur	Merge/separate features
Intensity	Contrast, brightness	Shift feature prominence
Morphological	Dilation, erosion	Modify connectivity and holes

maintain structural similarity for positive pairs while providing sufficient topological diversity for CL methods.

Designing such topology-aware augmentations involves three challenges. (1) We need to define a quantitative measure for topological changes after augmentations. (2) We need to identify which augmentation operations and their parameter settings produce controllable topological changes. (3) We need to establish optimal measure ranges for topology-weak versus topology-strong augmentations that balance topological similarity with sufficient diversity for effective TopoCL training.

For the first challenge, we define a relative bottleneck distance to quantify topological changes:

$$d_B^{\text{rel}}(\mathcal{A}, x) = \frac{d_B(\text{PD}(x), \text{PD}(\mathcal{A}(x)))}{\text{span}(\text{PD}(x))},$$

where $\text{PD}(x)$ denotes the persistence diagram of image x , \mathcal{A} is an augmentation operator, $\mathcal{A}(x)$ is the augmented version of image x , d_B is the bottleneck distance between PDs, and $\text{span}(\text{PD}(x)) = \max_{(b,d) \in \text{PD}(x)} |d - b|$ provides normalization to enable comparison across images with different topological scales, where (b, d) denotes the birth and death times of topological features. We compute d_B^{rel} separately for the H_0 and H_1 homology dimensions, and take the maximum as the overall topological change. Our d_B^{rel} measure is grounded in the stability theorem [11], which guarantees that augmentations with bounded intensity produce bounded changes in PDs.

To apply this measure effectively, we consider where to compute PDs. Computing d_B^{rel} on full medical images can include background noise and artifacts that obscure relevant topological changes. Thus, we compute PDs on regions of interest (ROIs) rather than on the full images. We extract ROIs using the Segment Anything Model (SAM) [23], which automatically identifies foreground regions containing relevant structures. Consistent with previous observations [10, 31], we find that persistent topological features concentrate within ROIs. This ROI-focused approach ensures that d_B^{rel} captures diagnostically relevant structural changes while filtering out background artifacts.

For the second challenge, we identify which operations and parameter settings produce controllable topological changes. However, exhaustive testing across all possible operations is infeasible. Thus, we categorize operations based on their mechanisms and topological effects,

and determine representative operations within each category. We identify five categories (Table 1): homeomorphisms (flips, rotations) preserve topology by reorienting pixel grids; boundary perturbations (Gaussian noise) alter sublevel set boundaries, potentially merging or splitting components; smoothing (Gaussian blur) merges nearby features or eliminates small structures; intensity transforms (contrast, brightness) shift filtration thresholds; morphological operations (dilation, erosion) directly modify pixel connectivity, adding or removing connections.

We systematically vary each operation’s intensity and measure d_B^{rel} across configurations, confirming positive correlation between intensity and d_B^{rel} . For example, increasing Gaussian noise can cause boundaries to fragment or merge, substantially increasing d_B^{rel} . We extend this to 2-3 operation combinations, identifying intensity ranges with varying topological changes.

For the third challenge, having determined how operations affect topology with d_B^{rel} , we identify optimal intensity ranges for topology-weak vs topology-strong augmentations. We consider various weak-strong range pairs by training TopoCL and measuring downstream linear probe performance (e.g., weak: 0-10%, strong: 10-20%; weak: 5-15%, strong: 15-25%). With systematic evaluations, we find that topology-weak augmentations should use operation intensities producing d_B^{rel} of 5-15%, and topology-strong augmentations should use intensities giving d_B^{rel} of 15-25%. This yields optimal performance across the datasets. Complete ablation results are given in Supplementary Material.

During training, we randomly select an operation combination and sample each operation’s intensity from validated ranges corresponding to the desired augmentation type: topology-weak augmentations use ranges producing d_B^{rel} of 5-15%, while topology-strong augmentations use 15-25%. For example, on ISIC2019, applying Flip with Gaussian noise $\sigma \in [0.05, 0.15]$ and contrast in $[0.1, 0.2]$ produces topology-weak augmentations. When this combination is selected, we sample noise and contrast from these ranges without computing d_B^{rel} at training time.

3.3. Hierarchical Topology Encoder

Having designed topology-aware augmentations, we consider how to encode PDs into learnable representations for contrastive learning. PDs are unordered sets of birth-death pairs, presenting a permutation invariance challenge similar to point cloud processing [32]. Moreover, persistent homology (PH) produces two types of features with distinct geometric semantics: H_0 captures connected components while H_1 captures holes; H_0 and H_1 exhibit geometric dependencies (e.g., holes are always bounded by connected components). We design a hierarchical topology encoder (H-Topo. Encoder) that addresses permutation invariance while respecting such structural distinctions and geomet-

ric relationships. Fig. 2(b) shows our H-Topo. Encoder architecture. Given a PD containing H_0 and H_1 features, we encode point sets through a PH Encoder, apply self-attention within each homology dimension, model inter-dimensional relationships via bidirectional cross-attention, aggregate features with max and mean pooling, and project to the final representation $\mathbf{t} \in \mathbb{R}^{256}$.

To process PDs, we adopt a PointNet-like network [32], called the PH Encoder. Since PDs have variable sizes, we select the top- k most persistent features ($k_{H_0} = 48$, $k_{H_1} = 96$), which capture nearly all significant topological structures across our benchmarks. We represent each selected birth-death pair as $\mathbf{p}_i = (b_i, d_i)$, where $i \in \{1, \dots, 144\}$ indexes the sequence of H_0 and H_1 features. To enable the encoder to distinguish between homology dimensions, we augment each pair with one-hot encoding: $\mathbf{e}_{n_i} = [1, 0]$ for the first 48 points (H_0) and $\mathbf{e}_{n_i} = [0, 1]$ for the remaining 96 points (H_1), giving $\tilde{\mathbf{p}}_i = [\mathbf{p}_i; \mathbf{e}_{n_i}] \in \mathbb{R}^4$. The PH Encoder processes all 144 $\tilde{\mathbf{p}}_i$ independently through four fully-connected layers ($4 \rightarrow 64 \rightarrow 128 \rightarrow 256 \rightarrow 384$). We then separate the encoded features into $\mathbf{h}_0 \in \mathbb{R}^{48 \times 384}$ and $\mathbf{h}_1 \in \mathbb{R}^{96 \times 384}$ for the two homology dimensions.

Given the embeddings \mathbf{h}_0 and \mathbf{h}_1 from the PH Encoder, we effectively learn topological representations that capture structural patterns. Medical image analysis commonly relies on two key characteristics. (1) Certain anatomical regions are more medically significant than others. For example, in tissue analysis, tumor regions are more diagnostically relevant than background tissues [27]. This requires our model to distinguish the importance of topological features within each homology dimension (e.g., H_0 features representing tumor regions vs background tissues). (2) Structural relationships among different types of anatomical features provide critical diagnostic information. For example, glandular lumens occurring within tumor regions indicate malignancy, while similar lumens within healthy tissues are benign [31]. Thus, our model should capture geometric dependencies between H_0 features (e.g., representing tumor regions or healthy tissues) and H_1 features (e.g., representing glandular lumens). We address both requirements through hierarchical attention mechanisms: self-attention within each dimension distinguishes feature importance, and cross-attention between dimensions captures geometric dependencies.

Specifically, as shown in Fig. 2(b), we first apply self-attention within each homology dimension with weighted residual connections: $\mathbf{h}'_0 = \mathbf{h}_0 + \lambda_0 \cdot \text{SelfAttn}(\mathbf{h}_0)$, $\mathbf{h}'_1 = \mathbf{h}_1 + \lambda_1 \cdot \text{SelfAttn}(\mathbf{h}_1)$, where $\lambda_0 = \lambda_1 = 0.5$ balance learned attention with the original features. Bidirectional cross-attention then models geometric relationships: $\mathbf{h}_0^{\leftrightarrow} = \text{CrossAttn}(\mathbf{h}'_0, \mathbf{h}'_1)$, $\mathbf{h}_1^{\leftrightarrow} = \text{CrossAttn}(\mathbf{h}'_1, \mathbf{h}'_0)$, where H_0 features serve as query and H_1 as key and value in $\mathbf{h}_0^{\leftrightarrow}$, and vice versa in $\mathbf{h}_1^{\leftrightarrow}$, modeling topological dependencies

Table 2. Dataset statistics for the five medical image datasets.

Dataset	Modality	Classes	Train / Test
PathMNIST	Colon Pathology	9	89,996 / 7,180
OCTMNIST	Retinal OCT	4	97,477 / 1,000
OrganSMNIST	Abdominal CT (Sagittal)	11	13,940 / 8,829
ISIC2019	Skin Lesion Dermoscopy	8	25,331 / 8,238
Kvasir	GI Endoscopy	8	3,200 / 800

such as hole containment within components. We concatenate the cross-attention outputs as $\mathbf{h}_{\text{cross}} = [\mathbf{h}_0^{\leftrightarrow}; \mathbf{h}_1^{\leftrightarrow}] \in \mathbb{R}^{144 \times 384}$, where $[\cdot; \cdot]$ denotes concatenation (Cross-Attn in Fig. 2(b)). Both self-attention and cross-attention use 4-head multi-head attention.

We aggregate features from self-attention ($\mathbf{h}'_0, \mathbf{h}'_1$) and cross-attention ($\mathbf{h}_{\text{cross}}$) using max and mean pooling. Max pooling captures the most salient topological structures, while mean pooling preserves global distributional information. Applying both pooling operations to each of these three feature sets yields six pooled vectors of 384 dimensions each, denoted as $\mathbf{h}_{\text{pool}} \in \mathbb{R}^{6 \times 384}$ (Max & Mean Pooling in Fig. 2(b)). A projection head (a three-layer MLP: $2304 \rightarrow 768 \rightarrow 512 \rightarrow 256$) then maps the flattened \mathbf{h}_{pool} to the final representation $\mathbf{t} \in \mathbb{R}^{256}$ (Proj Head in Fig. 2(b)). During pretraining, the H-Topo. Encoder is trained with the contrastive loss $\mathcal{L}_{\mathcal{M}}$.

3.4. Mixture-of-Experts Fusion

After independently pretraining the visual and topology encoders (Section 3.1), we jointly fine-tune them with a fusion module using contrastive learning. Existing fusion strategies include concatenation [29], gated fusion [2], cross-attention [41], etc., each assuming that a single strategy is optimal for all samples. However, medical images often exhibit substantial heterogeneity: texture-dominated samples (e.g., in dermoscopy images, pigmentation patterns are diagnostic) may benefit more from visual features, while structure-dominated samples (e.g., in histopathology, glandular connectivity is critical) require stronger topological signals [27]. Such diversities motivate the use of a Mixture-of-Experts (MoE) approach [36], which combines multiple fusion strategies rather than committing to a single strategy. We design five fusion experts covering diverse paradigms (vision-only, topology-only, concatenation, gated blending, and cross-modal interaction), enabling the model to learn sample-specific expert weights.

Fig. 2(a) illustrates the joint fine-tuning workflow with MoE fusion. Given an input image x , we apply topology-aware augmentations (Section 3.2) to generate two views x_{topo}^w and x_{topo}^s , and compute their PDs $\text{topo}^w = \text{PD}(x_{\text{topo}}^w)$ and $\text{topo}^s = \text{PD}(x_{\text{topo}}^s)$. The two pretrained encoders f_v and f_t process the augmented images and PDs, respectively. We project both encoder outputs to a shared 256-dimensional embedding space through separate 3-layer MLP projection heads, yielding visual features $\mathbf{f}^w, \mathbf{f}^s$ and topological fea-

Table 3. Performance comparison across five medical image datasets. The results show mean \pm standard deviation over five independent runs. Statistical significance is assessed via paired t-tests: ***: $p < 0.001$, **: $p < 0.01$, *: $p < 0.05$. \dagger indicates performance decrease. The Avg. columns report dataset-averaged metric values.

Method	Path		OrganS		OCT		ISIC		Kvasir		Avg.	
	ACC	AUC										
SimCLR [8]	92.57 \pm 0.31	99.12 \pm 0.11	77.12 \pm 0.26	96.41 \pm 0.26	69.41 \pm 0.56	91.83 \pm 0.43	66.04 \pm 2.29	88.01 \pm 1.11	74.33 \pm 1.28	95.89 \pm 0.76	75.89 \pm 0.51	94.25 \pm 0.11
+TopoCL	93.21 \pm 0.14	99.28 \pm 0.05	78.62 \pm 0.06	96.75 \pm 0.33	73.10 \pm 0.21	93.41 \pm 0.26	71.62 \pm 0.21	89.82 \pm 0.77	78.61 \pm 0.41	97.11 \pm 0.32	79.03 \pm 0.10	95.27 \pm 0.15
MoCo-v3 [9]	93.13 \pm 0.42	99.07 \pm 0.09	78.02 \pm 0.34	99.57 \pm 0.31	80.02 \pm 0.34	96.01 \pm 0.04	74.98 \pm 2.01	92.86 \pm 1.12	88.42 \pm 2.01	97.37 \pm 2.01	82.91 \pm 0.66	96.98 \pm 0.60
+TopoCL	94.55 \pm 0.20	99.24 \pm 0.09	80.58 \pm 0.09	98.75 \pm 0.21	82.09 \pm 0.26	97.09 \pm 0.13	78.44 \pm 0.83	93.26 \pm 0.97	91.17 \pm 0.83	98.81 \pm 0.46	85.37 \pm 0.11	97.43 \pm 0.27
BYOL [17]	93.42 \pm 0.09	99.31 \pm 0.14	76.41 \pm 0.19	97.33 \pm 0.08	76.02 \pm 0.26	95.89 \pm 0.25	73.82 \pm 3.19	90.75 \pm 0.79	85.67 \pm 0.98	96.91 \pm 0.13	81.07 \pm 0.49	96.04 \pm 0.20
+TopoCL	94.89 \pm 0.19	99.41 \pm 0.06	79.53 \pm 0.12	98.03 \pm 0.21	79.13 \pm 0.24	96.18 \pm 0.16	77.18 \pm 0.62	91.52 \pm 0.46	88.83 \pm 0.88	97.55 \pm 0.48	83.91 \pm 0.14	96.54 \pm 0.20
DINO [5]	91.92 \pm 0.15	98.99 \pm 0.18	71.11 \pm 0.31	95.39 \pm 0.08	61.21 \pm 0.33	91.27 \pm 0.16	63.24 \pm 2.45	85.28 \pm 0.89	71.42 \pm 1.86	96.99 \pm 0.27	71.78 \pm 0.50	93.58 \pm 0.19
+TopoCL	94.57 \pm 0.08	99.38 \pm 0.05	77.21 \pm 0.17	96.96 \pm 0.13	65.03 \pm 0.19	93.87 \pm 0.15	67.08 \pm 0.17	88.38 \pm 0.59	77.99 \pm 1.27	98.31 \pm 0.25	76.38 \pm 0.30	95.38 \pm 0.17
Barlow [44]	93.09 \pm 0.11	99.41 \pm 0.06	76.76 \pm 0.26	98.13 \pm 0.09	78.08 \pm 0.49	96.91 \pm 0.15	62.70 \pm 1.41	87.11 \pm 0.26	73.41 \pm 1.29	97.57 \pm 0.22	76.81 \pm 0.37	95.83 \pm 0.08
+TopoCL	94.91 \pm 0.05	99.52 \pm 0.04	79.69 \pm 0.09	98.75 \pm 0.11	80.51 \pm 0.28	97.28 \pm 0.18	67.22 \pm 0.23	89.02 \pm 0.45	78.08 \pm 1.08	98.13 \pm 0.41	80.08 \pm 0.20	96.54 \pm 0.08

tures $\mathbf{t}^w, \mathbf{t}^s$ (Vis.-Topo. Embed in Fig. 2(a)). A multi-gating network processes the concatenated features $[\mathbf{f}; \mathbf{t}]$ to compute sample-specific weights, $\text{gate}^w, \text{gate}^s \in \mathbb{R}^5$. In parallel, the five fusion experts process the features based on their respective strategies (detailed below). The expert outputs are combined through weighted summation using the gate weights (Weighted Sum in Fig. 2(a)), and a projection head produces the final embeddings $\mathbf{z}^w, \mathbf{z}^s \in \mathbb{R}^{256}$.

To enable this sample-adaptive fusion, we design five expert networks with distinct fusion strategies. For clarity, we describe the operations for a single view; the same approach applies to both views. All experts have access to both projected visual features \mathbf{f} and topological features \mathbf{t} (corresponding to $\mathbf{f}^w, \mathbf{t}^w$ or $\mathbf{f}^s, \mathbf{t}^s$), but process them with their own strategies. **Expert 1**, Vis.-Only (\mathbf{e}_1), and **Expert 2**, Topo.-Only (\mathbf{e}_2), process single feature types: $\mathbf{e}_1 = \text{MLP}(\mathbf{f})$, $\mathbf{e}_2 = \text{MLP}(\mathbf{t})$, allowing the model to rely solely on visual or topological information. **Expert 3**, Concat (\mathbf{e}_3), processes concatenated features: $\mathbf{e}_3 = \text{MLP}([\mathbf{f}; \mathbf{t}])$, capturing additive interactions. **Expert 4**, Gated Blending (\mathbf{e}_4), learns sample-specific blending: $\mathbf{g} = \sigma(\text{MLP}([\mathbf{f}; \mathbf{t}]))$, $\mathbf{e}_4 = \text{MLP}(\mathbf{g} \odot \mathbf{f} + (1 - \mathbf{g}) \odot \mathbf{t})$, where σ is sigmoid and \odot denotes element-wise multiplication. **Expert 5**, Cross-Attn (\mathbf{e}_5), applies bidirectional cross-attention with residual connections: $\mathbf{f}' = \mathbf{f} + \text{CrossAttn}(Q = \mathbf{f}, KV = \mathbf{t})$, $\mathbf{t}' = \mathbf{t} + \text{CrossAttn}(Q = \mathbf{t}, KV = \mathbf{f})$, $\mathbf{e}_5 = \text{MLP}([\mathbf{f}'; \mathbf{t}'])$, where Q denotes query and KV denotes key-value pairs in the attention mechanism. All experts use 3-layer MLPs and output 512-dimensional representations $\mathbf{e}_i \in \mathbb{R}^{512}$.

These expert outputs are combined with a gating mechanism. A multi-gating network (a 3-layer MLP: $512 \rightarrow 256 \rightarrow 128 \rightarrow 5$) takes concatenated features $[\mathbf{f}; \mathbf{t}]$ as input and produces normalized weights: $\text{gate} = \text{softmax}(\text{Multi-Gating}([\mathbf{f}; \mathbf{t}])) \in \mathbb{R}^5$. The fused representation is obtained via weighted sum: $\mathbf{h} = \sum_{i=1}^5 \text{gate}_i \cdot \mathbf{e}_i \in \mathbb{R}^{512}$, which a projection head then maps to $\mathbf{z} \in \mathbb{R}^{256}$

(Proj Head in Fig. 2(a)). During joint fine-tuning, both views produce embeddings $\mathbf{z}^w, \mathbf{z}^s$, optimized using the contrastive objective in Section 3.1. During inference, given a single image, we extract its ROIs, compute the PD without augmentations, process the image through f_v and the PD through f_t respectively, and fuse the projected features through the gating mechanism and experts to produce the final representation for downstream tasks.

4. Experiments

Datasets. We evaluate on five medical image classification datasets covering diverse modalities and anatomical regions (Table 2): PathMNIST, OCTMNIST, OrganSMNIST, ISIC2019, and Kvasir. All images are preprocessed to 224×224 following MedMNIST v2 protocols [43].

Baseline Methods. We integrate TopoCL with five representative CL methods: SimCLR [8], MoCo-v3 [9], BYOL [17], DINO [5], and Barlow Twins [44]. All methods use ResNet-50 as the visual encoder backbone and are trained for 150 epochs.

Evaluation Protocol. Following standard self-supervised evaluation [5, 8], we assess representation quality via linear probing: a linear classifier is trained on frozen encoder features for 100 epochs and evaluated on the test set. We report accuracy (ACC) and macro-averaged AUC, averaged over five runs with statistical significance via paired t-tests.

Implementation Details. We apply SAM-ViT-H [23] to extract ROIs and compute PDs with GUDHI [12], retaining top-48 H_0 and top-96 H_1 features. The Hierarchical Topology Encoder uses 4-head attention with dimension 384. Models are trained on H100 GPUs with batch size 256, AdamW optimizer (learning rate 3×10^{-4}), and cosine annealing. Full details are in Supplementary Material.

4.1. Main Results

Table 3 presents comprehensive results on integrating our TopoCL with five CL methods and five medical image

Table 4. Ablation of topology-aware augmentation configurations using MoCo-v3+TopoCL. ACC results (%) are reported.

Configuration	OrganS	ISIC	Kvasir
TopoCL (weak+strong)	75.51 \pm 1.56	72.92 \pm 2.32	84.63 \pm 1.85
TopoCL (full image)	76.34 \pm 1.46	74.35 \pm 1.58	87.41 \pm 1.88
TopoCL (topo-weak+topo-weak)	78.98 \pm 0.37	76.39 \pm 0.55	90.01 \pm 0.28
TopoCL (topo-strong+topo-strong)	78.02 \pm 0.68	75.99 \pm 1.02	89.64 \pm 0.91
TopoCL (topo-weak+topo-strong)	80.58\pm0.99	78.44\pm0.83	91.17\pm0.43

datasets. Averaged across all datasets, TopoCL consistently improves the baseline performance, with ACC gains ranging from +2.46% to +4.60% and AUC gains from +0.45% to +1.80%, giving overall average improvements of +3.26% ACC and +0.90% AUC. Statistical analysis via paired t-tests shows strong statistical significance: 86% (43/50) of individual dataset-metric comparisons and 90% (9/10) of dataset-averaged metrics achieve statistical significance ($p < 0.05$), with 80% of the averaged metrics reaching $p < 0.001$. Importantly, observe that TopoCL benefits all five CL methods, with every baseline showing positive average improvements in both ACC and AUC.

TopoCL yields particularly strong results with DINO, achieving the largest average gains (+4.60% ACC, +1.80% AUC) with statistical significance across all ten dataset-metric combinations. Dataset-wise, OCT and Kvasir show substantial improvements (average gains of +3.02% and +4.29% ACC, respectively), with beneficial structural patterns from topological features. ISIC exhibits higher variance due to skin lesion heterogeneity, yielding some moderate improvements despite consistent positive trends.

One notable exception occurs with MoCo-v3 on OrganSMNIST, where AUC decreases from 99.57% to 98.75% ($p = 0.023$) despite a considerable ACC improvement (+2.56%, $p < 0.001$). This suggests a trade-off in the near-saturated situations (baseline AUC > 99.5%), where topological features help optimize classification performance at the expense of ranking confidence. Nevertheless, these results validate that TopoCL provides robust and statistically significant improvements across diverse CL methods and medical imaging modalities.

4.2. Topology-Aware Augmentation Design Choices

We evaluate topology-aware augmentation design choices using MoCo-v3+TopoCL on three datasets. We compare five configurations: (a) *weak+strong*: standard visual weak/strong augmentations (as in the baseline MoCo-v3); (b) *full image*: topology-aware weak/strong augmentations with PDs computed on the entire images instead of SAM-extracted ROIs; (c) *topo-weak+topo-weak* and (d) *topo-strong+topo-strong*: symmetric topology-aware augmentation pairs (both views use the same augmentation strength) on SAM-extracted ROIs; (e) *topo-weak+topo-strong*: mixed topology-aware augmentation pairs (different augmentation strengths) on SAM-extracted ROIs.

Table 5. Ablation with SimCLR+TopoCL on three datasets. We evaluate: (1) pretraining strategies (rows 1-3); (2) hierarchical topology encoder components (rows 4-6); (3) MoE expert choices (rows 7-11). ACCs (%) averaged over five runs are reported.

Configuration	Path	OrganS	OCT
w/o pretraining	68.98 \pm 1.43	50.61 \pm 0.87	48.72 \pm 1.77
w/o vis. pretrain	81.53 \pm 0.98	64.72 \pm 1.21	66.98 \pm 0.83
w/o topo. pretrain	87.64 \pm 0.92	72.56 \pm 1.11	69.37 \pm 0.89
w/o hier. attn	86.51 \pm 0.93	72.85 \pm 0.76	67.62 \pm 1.03
w/o self-attn	91.24 \pm 0.85	76.03 \pm 0.56	70.28 \pm 0.66
w/o cross-attn	87.59 \pm 0.85	74.66 \pm 0.71	69.38 \pm 0.57
w/o vis-only expert	92.59 \pm 0.43	77.47 \pm 0.51	71.85 \pm 0.34
w/o topo-only expert	93.01 \pm 0.18	78.15 \pm 0.11	72.53 \pm 0.25
w/o concat expert	92.88 \pm 0.58	78.05 \pm 0.43	72.68 \pm 0.41
w/o gated expert	92.05 \pm 0.56	76.89 \pm 0.47	71.63 \pm 0.66
w/o cross-attn expert	91.75 \pm 0.48	76.03 \pm 0.56	70.95 \pm 0.48
Full model	93.21 \pm 0.14	78.62 \pm 0.06	73.10 \pm 0.21

In Table 4, we observe: (1) Replacing standard visual augmentations with topology-aware augmentations yields substantial gains; the mixed *topo-weak+topo-strong* pairing achieves the best results across the datasets. This supports our premise that explicitly controlling topological perturbations preserves semantically meaningful structures. (2) Computing PDs on SAM-extracted ROIs outperforms computing them on full images, indicating that focusing topology measurements on relevant anatomy (rather than background) enables more precise topological control. (3) Symmetric topology-aware pairs (*topo-weak+topo-weak* or *topo-strong+topo-strong*) improve over standard visual augmentations, but the mixed pairing provides the most informative contrast, likely because it exposes the encoder to controlled yet complementary topology variations.

4.3. Ablation Studies

To validate the effect of each design component, we conduct systematic ablations with SimCLR+TopoCL on three datasets (Table 5). We evaluate the pretraining strategies, topology encoder architecture, and MoE expert choices.

Pretraining Strategies. Visual and topological pretraining are both essential; their removal causes severe degradation (68.98% vs 93.21% on PathMNIST). Visual pretraining has a much larger impact (performance drops to 81.53%) than topological pretraining (87.64%), confirming that visual features provide primary representations and topological features offer complementary structural information.

Topology Encoder Architecture. The hierarchical design is critical; its complete removal drops the performance by 6.70% on PathMNIST. Cross-attention (87.59%) is more important than self-attention (91.24%), as it captures relationships between connected components (H_0) and holes (H_1), validating our hierarchical integration strategy.

MoE Expert Effects. All five experts contribute to the performance, with fusion-based experts being most effective: Cross-attention expert (1.73% average drop when re-

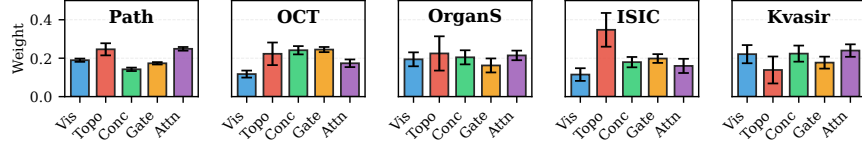


Figure 3. Expert gating analysis for TopoCL integrated with BYOL on five datasets. Error bars show standard deviation across test samples. Five experts: visual-only (Vis), topology-only (Topo), concatenation (Conc), gated blending (Gate), and cross-attention (Attn).

Table 6. Computational cost comparison on ISIC2019.

Method	Train (h)	Params (M)	FLOPs (G)	Tput.	Overhead
SimCLR	1.58	24.89	4.11	668	-
+TopoCL	1.84	31.08	6.11	574	+16%
BYOL	1.72	53.28	2.88	614	-
+TopoCL	1.96	60.48	4.58	539	+14%
DINO	1.79	45.16	5.23	590	-
+TopoCL	1.99	51.00	7.03	531	+11%
Barlow	1.28	24.89	4.57	825	-
+TopoCL	1.51	31.08	6.54	700	+18%
MoCo-v3	1.72	52.89	3.09	614	-
+TopoCL	1.83	59.73	5.33	577	+6%

Table 7. Training and inference cost breakdown for SimCLR+TopoCL on ISIC2019.

Component	Training		Inference	
	Time (h)	%	Params (M)	FLOPs (G)
Visual Encoder	1.06	57.61	24.03	4.11
Topo Encoder	0.35	19.02	3.83	1.99
MoE+Proj	0.43	23.37	3.23	0.01
Total	1.84	100.0	31.08	6.11

moved), gated expert (1.45%), visual-only expert (1.01%), concat expert (0.44%), and topology-only expert (0.41%). The finding of fusion experts outweighing feature-specific experts validates our MoE design, in which topological information is effectively leveraged when adaptively integrated with visual features rather than used in isolation.

4.4. Computational Cost Analysis

Table 6 analyzes the computational overhead of TopoCL with the five CL methods. Integrating topology-aware augmentation and MoE fusion adds modest overhead: Training time increases by 6-18%, depending on the method (13% average), with SimCLR+TopoCL completing 150 epochs in 1.84 hours on H100. The parameter count increases by 6.5M on average (17%), while FLOPs increase by ~ 2 GFLOPs (51% average increase). The throughput reduction averages 12%, which is acceptable for medical imaging applications where training is typically conducted once.

Table 7 provides cost breakdown for SimCLR+TopoCL. The Visual Encoder (24.03M parameters) refers to the ResNet-50 backbone shared with the baseline SimCLR. The baseline’s parameter count of 24.89M in Table 6 includes an additional 0.86M projection head, which TopoCL replaces with the Topo Encoder (3.83M) and MoE+Proj (3.23M) modules. The visual encoder dominates both training time (57.61%) and inference cost (67% of FLOPs), while the

topology encoder contributes 19% of training time and 33% of inference FLOPs. For deployment, topology features can be precomputed offline (0.64 h for ISIC2019), reducing inference overhead to primarily the MoE+Proj component and making TopoCL practical for clinical applications.

4.5. Expert Gating Analysis

Fig. 3 reveals dataset-specific gating patterns for BYOL. PathMNIST strongly prefers topology-only and cross-attention experts, indicating histopathology benefits from both standalone topological features and their integration with visual features. OCTMNIST and OrganSMNIST exhibit balanced gating, indicating retinal OCT and abdominal CT structures require diverse fusion strategies. ISIC2019 demonstrates the strongest topology-only preference, likely because skin lesion boundaries encoded by PH are particularly discriminative. Kvasir shows balanced weights with a slight emphasis on concatenation and visual-only experts.

The topology-only expert receives varying importance across the datasets (high on ISIC2019, lower on the others), demonstrating adaptive determination of when standalone topological features are most valuable vs when integration through fusion experts is preferred. While Table 3 shows that topological features improve all methods, this analysis reveals that an optimized fusion strategy is dataset-dependent. The multi-gating network learns these preferences without supervision, validating TopoCL’s adaptive design. Similar patterns for other CL methods (see Supplementary Material) demonstrate broad generalization.

5. Conclusions

In this paper, we introduced TopoCL, a new general topological contrastive learning framework for medical imaging that augments standard contrastive learning with explicit topological preservation. Our method combines topology-aware augmentations calibrated via relative bottleneck distance of persistence diagrams, a Hierarchical Topology Encoder that captures both H_0 and H_1 topological features, and an adaptive Mixture-of-Experts module that fuses visual and topological representations. Extensive experiments on five medical image benchmarks using five representative CL baselines (SimCLR, MoCo-v3, BYOL, DINO, and Barlow Twins) showed that TopoCL improves the average accuracy by +3.26% with strong statistical significance, confirming that topological cues provide complementary and robust supervisory signals.

References

- [1] Diego Adame, Jose A Nunez, Fabian Vazquez, Nayeli Gurrola, Huimin Li, Haoteng Tang, Bin Fu, and Pengfei Gu. Topo-VM-UNetV2: Encoding topology into vision Mamba UNet for polyp segmentation. In *Proceedings of the IEEE 38th International Symposium on Computer-Based Medical Systems*, pages 258–263, 2025.
- [2] John Arevalo, Thamar Solorio, Manuel Montes-y Gómez, and Fabio A González. Gated multimodal units for information fusion. *arXiv preprint arXiv:1702.01992*, 2017.
- [3] Shekoofeh Azizi, Basil Mustafa, Fiona Ryan, Zachary Beaver, Jan Freyberg, Jonathan Deaton, Aaron Loh, Alan Karthikesalingam, Simon Kornblith, Ting Chen, Vivek Natarajan, and Mohammad Norouzi. Big self-supervised models advance medical image classification. In *Proceedings of the IEEE/CVF International Conference on Computer Vision*, pages 3478–3488, 2021.
- [4] Gabriele Campanella, Matthew G Hanna, Luke Geneslaw, Allen Mirafior, Vitor Werneck Krauss Silva, Klaus J Busam, Edi Brogi, Victor E Reuter, David S Klimstra, and Thomas J Fuchs. Clinical-grade computational pathology using weakly supervised deep learning on whole slide images. *Nature Medicine*, 25(8):1301–1309, 2019.
- [5] Mathilde Caron, Hugo Touvron, Ishan Misra, Hervé Jégou, Julien Mairal, Piotr Bojanowski, and Armand Joulin. Emerging properties in self-supervised Vision Transformers. In *Proceedings of the IEEE/CVF International Conference on Computer Vision*, pages 9650–9660, 2021.
- [6] Mathieu Carrière, Frédéric Chazal, Yuichi Ike, Théo Lacombe, Martin Royer, and Yuhei Umeda. PersLay: A neural network layer for persistence diagrams and new graph topological signatures. In *Proceedings of the International Conference on Artificial Intelligence and Statistics*, pages 2786–2796, 2020.
- [7] Erin W Chambers and Guangyu Meng. A stable and theoretically grounded Gromov-Wasserstein distance for Reeb graph comparison using persistence images. *arXiv preprint arXiv:2507.01171*, 2025.
- [8] Ting Chen, Simon Kornblith, Mohammad Norouzi, and Geoffrey Hinton. A simple framework for contrastive learning of visual representations. In *Proceedings of the International Conference on Machine Learning*, pages 1597–1607, 2020.
- [9] Xinlei Chen, Saining Xie, and Kaiming He. An empirical study of training self-supervised Vision Transformers. In *Proceedings of the IEEE/CVF International Conference on Computer Vision*, pages 9640–9649, 2021.
- [10] James R Clough, Nicholas Byrne, Ilkay Oksuz, Veronika A Zimmer, Julia A Schnabel, and Andrew P King. A topological loss function for deep-learning based image segmentation using persistent homology. *IEEE Transactions on Pattern Analysis and Machine Intelligence*, 44(12):8766–8778, 2020.
- [11] David Cohen-Steiner, Herbert Edelsbrunner, and John Harer. Stability of persistence diagrams. In *Proceedings of the 21st Annual Symposium on Computational Geometry*, pages 263–271, 2005.
- [12] Pawel Dlotko. Cubical complex. In *GUDHI User and Reference Manual*. GUDHI Editorial Board, 3.11.0 edition, 2025.
- [13] Herbert Edelsbrunner and John Harer. *Computational Topology: An Introduction*. American Mathematical Society, 2010.
- [14] Christopher W Elston and Ian O Ellis. Pathological prognostic factors in breast cancer. I. the value of histological grade in breast cancer: Experience from a large study with long-term follow-up. *Histopathology*, 19(5):403–410, 1991.
- [15] William Fedus, Barret Zoph, and Noam Shazeer. Switch Transformers: Scaling to trillion parameter models with simple and efficient sparsity. *Journal of Machine Learning Research*, 23(120):1–39, 2022.
- [16] Yang Gao, Oscar Beijbom, Ning Zhang, and Trevor Darrell. Compact bilinear pooling. In *Proceedings of the IEEE Conference on Computer Vision and Pattern Recognition*, pages 317–326, 2016.
- [17] Jean-Bastien Grill, Florian Strub, Florent Altché, Corentin Tallec, Pierre H Richemond, Elena Buchatskaya, Carl Doersch, Bernardo Avila Pires, Zhaohan Daniel Guo, Mohammad Gheshlaghi Azar, et al. Bootstrap Your Own Latent: A new approach to self-supervised learning. In *Proceedings of the Conference on Neural Information Processing Systems*, pages 21271–21284, 2020.
- [18] Pengfei Gu, Huimin Li, Yejia Zhang, Chaoli Wang, and Danny Z Chen. Self pre-training with topology-and spatiality-aware masked autoencoders for 3D medical image segmentation. In *Proceedings of the IEEE International Conference on Bioinformatics and Biomedicine*, pages 3608–3613, 2025.
- [19] Pengfei Gu, Hongxiao Wang, Yejia Zhang, Huimin Li, Chaoli Wang, and Danny Z Chen. TopoImages: Incorporating local topology encoding into deep learning models for medical image classification. In *Proceedings of the 33rd ACM International Conference on Multimedia*, pages 1938–1947, 2025.
- [20] Pengfei Gu, Huimin Li, Haoteng Tang, Dongkuan Xu, Erik Enriquez, DongChul Kim, Bin Fu, and Danny Z Chen. Integrating multi-scale and multi-filtration topological features for medical image classification. In *Proceedings of the IEEE/CVF Winter Conference on Applications of Computer Vision*, pages 8660–8669, 2026.
- [21] Kaiming He, Haoqi Fan, Yuxin Wu, Saining Xie, and Ross Girshick. Momentum contrast for unsupervised visual representation learning. In *Proceedings of the IEEE/CVF Computer Vision and Pattern Recognition*, pages 9729–9738, 2020.
- [22] Jeremy Irvin, Pranav Rajpurkar, Michael Ko, Yifan Yu, Silvana Ciurea-Ilcus, Chris Chute, Henrik Marklund, Behzad Haghgoo, Robyn Ball, Katie Shpanskaya, et al. CheXpert: A large chest radiograph dataset with uncertainty labels and expert comparison. In *Proceedings of the AAAI Conference on Artificial Intelligence*, pages 590–597, 2019.
- [23] Alexander Kirillov, Eric Mintun, Nikhila Ravi, Hanzi Mao, Chloe Rolland, Laura Gustafson, Tete Xiao, Spencer Whitehead, Alexander C Berg, Wan-Yen Lo, et al. Segment anything. In *Proceedings of the IEEE/CVF International Conference on Computer Vision*, pages 4015–4026, 2023.

- [24] Peter Lawson, Andrew B Sholl, J Quincy Brown, Britany Terese Fasy, and Carola Wenk. Persistent homology for the quantitative evaluation of architectural features in prostate cancer histology. *Scientific Reports*, 9(1):1–12, 2019.
- [25] Peixian Liang, Yifan Ding, Yizhe Zhang, Jianxu Chen, Hao Zheng, Hongxiao Wang, Yejia Zhang, Guangyu Meng, Tim Weninger, Michael Niemier, X. Sharon Hu, and Danny Z Chen. Cell instance segmentation: The devil is in the boundaries. *IEEE Transactions on Medical Imaging*, pages 1–1, 2025.
- [26] Paul Pu Liang, Amir Zadeh, and Louis-Philippe Morency. Foundations & trends in multimodal machine learning: Principles, challenges, and open questions. *ACM Computing Surveys*, 56(10):1–42, 2024.
- [27] Geert Litjens, Thijs Kooi, Babak Ehteshami Bejnordi, Arnaud Arindra Adiyoso Setio, Francesco Ciompi, Mohsen Ghafoorian, Jeroen Awm Van Der Laak, Bram Van Ginneken, and Clara I Sánchez. A survey on deep learning in medical image analysis. *Medical Image Analysis*, 42:60–88, 2017.
- [28] Jiasen Lu, Dhruv Batra, Devi Parikh, and Stefan Lee. ViLBERT: Pretraining task-agnostic visiolinguistic representations for vision-and-language tasks. *Advances in Neural Information Processing Systems*, 32, 2019.
- [29] Jiquan Ngiam, Aditya Khosla, Mingyu Kim, Juhan Nam, Honglak Lee, Andrew Y Ng, et al. Multimodal deep learning. In *Proceedings of the International Conference on Machine Learning*, pages 689–696, 2011.
- [30] Yaopeng Peng, Hongxiao Wang, Milan Sonka, and Danny Z Chen. PHG-Net: Persistent homology guided medical image classification. In *Proceedings of the IEEE/CVF Winter Conference on Applications of Computer Vision*, pages 7583–7592, 2024.
- [31] Talha Qaiser, Yee-Wah Tsang, Daiki Taniyama, Naoya Sakamoto, Kazuaki Nakane, David Epstein, and Nasir Rajpoot. Fast and accurate tumor segmentation of histology images using persistent homology and deep convolutional features. *Medical Image Analysis*, 55:1–14, 2019.
- [32] Charles R Qi, Hao Su, Kaichun Mo, and Leonidas J Guibas. PointNet: Deep learning on point sets for 3D classification and segmentation. In *Proceedings of the IEEE Conference on Computer Vision and Pattern Recognition*, pages 652–660, 2017.
- [33] Pranav Rajpurkar, Jeremy Irvin, Kaylie Zhu, Brandon Yang, Hershel Mehta, Tony Duan, Daisy Ding, Aarti Bagul, Curtis Langlotz, Katie Shpanskaya, et al. CheXNet: Radiologist-level pneumonia detection on chest X-rays with deep learning. *arXiv preprint arXiv:1711.05225*, 2017.
- [34] Carlos Riquelme, Joan Puigcerver, Basil Mustafa, Maxim Neumann, Rodolphe Jenatton, André Susano Pinto, Daniel Keysers, and Neil Houlsby. Scaling vision with sparse mixture of experts. *Advances in Neural Information Processing Systems*, 34:8583–8595, 2021.
- [35] Ramprasaath R Selvaraju, Michael Cogswell, Abhishek Das, Ramakrishna Vedantam, Devi Parikh, and Dhruv Batra. Grad-CAM: Visual explanations from deep networks via gradient-based localization. In *Proceedings of the IEEE International Conference on Computer Vision*, pages 618–626, 2017.
- [36] Noam Shazeer, Azalia Mirhoseini, Krzysztof Maziarz, Andy Davis, Quoc Le, Geoffrey Hinton, and Jeff Dean. Outrageously large neural networks: The sparsely-gated mixture-of-experts layer. *arXiv preprint arXiv:1701.06538*, 2017.
- [37] Saeed Shurrah and Rehab Duwairi. Self-supervised learning methods and applications in medical imaging analysis: A survey. *PeerJ Computer Science*, 8:e1045, 2022.
- [38] Yashbir Singh, Colleen M Farrelly, Quincy A Hathaway, Tim Leiner, Jaidip M Jagtap, Gunnar E Carlsson, and Bradley J Erickson. Topological data analysis in medical imaging: Current state of the art. *Insights into Imaging*, 14(1):58, 2023.
- [39] Philipp Tschandl, Cliff Rosendahl, and Harald Kittler. The HAM10000 dataset, a large collection of multi-source dermatoscopic images of common pigmented skin lesions. *Scientific Data*, 5:180161, 2018.
- [40] Tao Tu, Shekoofeh Azizi, Danny Driess, Mike Schaeckermann, Mohamed Amin, Pi-Chuan Chang, Andrew Carroll, Charles Lau, Ryutaro Tanno, Ira Ktena, et al. Towards generalist biomedical AI. *NEJM AI*, 1(3):AIoa2300138, 2024.
- [41] Ashish Vaswani, Noam Shazeer, Niki Parmar, Jakob Uszkoreit, Llion Jones, Aidan N Gomez, Łukasz Kaiser, and Illia Polosukhin. Attention is all you need. *Advances in Neural Information Processing Systems*, 30, 2017.
- [42] Hubert Wagner, Chao Chen, and Erald Vućini. Efficient computation of persistent homology for cubical data. In *Proceedings of the Topological Methods in Data Analysis and Visualization II: Theory, Algorithms, and Applications*, pages 91–106. Springer, 2011.
- [43] Jiancheng Yang, Rui Shi, Donglai Wei, Zequan Liu, Lin Zhao, Bilian Ke, Hanspeter Pfister, and Bingbing Ni. MedMNIST v2-a large-scale lightweight benchmark for 2D and 3D biomedical image classification. *Scientific Data*, 10(1):41, 2023.
- [44] Jure Zbontar, Li Jing, Ishan Misra, Yann LeCun, and Stéphane Deny. Barlow Twins: Self-supervised learning via redundancy reduction. In *Proceedings of the International Conference on Machine Learning*, pages 12310–12320, 2021.
- [45] Chao Zhang, Zichao Yang, Xiaodong He, and Li Deng. Multimodal intelligence: Representation learning, information fusion, and applications. *IEEE Journal of Selected Topics in Signal Processing*, 14(3):478–493, 2020.
- [46] Sheng Zhou, Hongjia Xu, Zhuonan Zheng, Jiawei Chen, Zhao Li, Jiajun Bu, Jia Wu, Xin Wang, Wenwu Zhu, and Martin Ester. A comprehensive survey on deep clustering: Taxonomy, challenges, and future directions. *ACM Computing Surveys*, 57(3):1–38, 2024.